IEEE Access
Multidisciplinary ⋮ Rapid Review ⋮ Open Access Journal

Received 13 October 2023, accepted 7 November 2023, date of publication 13 November 2023,
date of current version 20 November 2023.

Digital Object Identifier 10.1109/ACCESS.2023.3332485

RESEARCH ARTICLE

Characterising the Photonic-Assisted Coherent Free-Space Link of Sub-THz Data Transmission

MOHANAD DAWOOD AL-DABBAGH[1], (Member, IEEE), JESSICA SMITH[2], THOMAS KLEINE-OSTMANN[1], MIRA NAFTALY[2], AND IRSHAAD FATADIN[2], (Senior Member, IEEE)

[1]Physikalisch-Technische Bundesanstalt (PTB), 38116 Braunschweig, Germany
[2]National Physical Laboratory, TW11 0LW Teddington, U.K.

Corresponding author: Mohanad Dawood Al-Dabbagh (mohanad.dabbagh@ieee.org)

This work was supported in part by the German Research Foundation (DFG) through the Meteracom Project (Metrology for THz Communications) under Grant FOR2863; and in part by the U.K. Government's Department for Science, Innovation and Technology (DSIT), National Physical Laboratory (NPL).

ABSTRACT This study demonstrates a measurement setup of an over-the-air (OTA) sub-THz link using a hybrid system of transmission comprising standard optical communications components and propagating the signal over 6 meters. The emitter was a p-i-n photodiode (PIN-PD), and the receiver was a sub-harmonic down-converter. The transmission testbed for the frequencies between 240 GHz to 300 GHz was characterised. Key parameters including the optical frequency, frequency hopping, the direct current (DC) bias of the emitter, the equalisation taps, and the digital signal processing stages were examined to optimise performance. An error-free 25.6 Gbit/s QPSK signal was achieved. A 16-QAM characterisation investigated the power combination from the two optical branches fed to the photodiode (PD) and its influence on the error vector magnitude (EVM) of the in-phase and quadrature (IQ) amplitude linearity and the probability density estimate. An optimum 16-QAM constellation was achieved using power combination of 5 mW and 10 mW for the optical modulator and optical carrier power, respectively. Finally, an image transmission of 24 data packets was performed and achieved error-free QPSK image reception at 25 Gbit/s.

INDEX TERMS 6G mobile communication, electromagnetic radiation, free-space, image transmission, photodiodes, terahertz communications.

I. INTRODUCTION

Wireless communications have traditionally been dominated by electronic systems. The electronic systems circuit design can be compact, which is beneficial for end-user devices, among other applications [1], [2], [3], [4], [5]. However, this technology is restricted by the limited bandwidth that its components can handle and the need for multiple circuits to cover different frequencies with adequate bandwidth for the application. Furthermore, purely electronic systems might be limited by noise, waveguide losses and power consumption. The limitations of electronics-based systems and the shift towards sub-THz frequencies have made optical systems an attractive solution. In the last decade this has spurred studies on radio over fibre and wireless transmission-based photonic systems, with many high-speed demonstrations in the WR-10 (75 – 110) GHz and WR-06 (110 – 170) GHz bands and, most recently, in the WR03 (220 – 325) GHz band [6], [7], [8].

Photomixers can efficiently provide an extended wide bandwidth of up to 3 THz, which electrical systems struggle to achieve. However, photomixer technology is expensive, and designing compact systems for users is challenging. Nevertheless, photomixer technology can be employed in hybrid systems for access points by taking advantage of their wide bandwidth. This type of photonic emitter has previously been used for the 300 GHz region [9], employing a combination with electronic in-phase and quadrature (IQ) receivers.

Presented here is the characterization of a hybrid optical and RF sub-THz over-the-air (OTA) system. This characterization involved separate studies on different aspects of the

The associate editor coordinating the review of this manuscript and approving it for publication was Wenxin Liu.

setup. We characterised different sub-THz frequencies within the WR03 band using quadrature phase shift keying (QPSK). The study also involved measuring the error vector magnitude (EVM) and the received signal strength. A p-i-n photodiode (PIN-PD) emitter was used to propagate the sub-THz signal.

First, the beam profile was investigated at three locations on the beam path via the knife edge method using a pyro-electric thin-film (PTF) detector placed at the receiver's focal point. We sampled the beam by translating a metal blade perpendicular to the beam axis in linear incremental steps.

It is important to investigate the beam profile to map the signal distribution along the beam path and determine if frequency selection influences the signal profile that the emitter radiates and if it affects the aligned beam. For systems potentially employing diffraction optics in the beam path, this is crucial. Parabolic mirrors were used to collimate the emitted beam and achieved the desired transmission distance of 6 meters. The radiation pattern of PIN-PD emitters and different antenna designs internal to the emitters have been investigated in [10], [11], and [12].

Next, we examined the influence of the choice of laser source wavelength on the received signal. This is because the signal strength and stability of a laser can differ [13], creating changes in the transmitter and receiver signal strength and data reception. Different optical frequencies in a 2.5 THz range were measured. Frequency changes in the carrier and modulated signals propagating through different components can influence the down-converted signal and change the output signal and beam profile of the emitter [14].

Then, we examined frequency hopping and its influence on the stability of data transmission in the measurement setup. The effect of the stability and frequency hopping of the laser on the received signal was examined by calculating the intermediate frequency (IF) offset slope over time and the influence of the frequency offset on the recovery of the received signal. A frequency offset estimation step was also required to aid digital signal processing (DSP). Cost-effective semiconductor lasers are used in a variety of applications. Some suffer from mode hopping, the effect of which has been reported in [15].

We then examined the influence of the external bias voltage of the emitter on the propagated signal and if the bias voltage would linearly affect the received signal at three selected voltages. The output current flowing through the emitter's antenna can be controlled by the PD bias voltage. The PD bias determines how a device responds to an optical signal; such as whether the output current is linear with the bias voltage. The output power of a PIN-PD at different DC biases is found in literature, and has been measured at frequencies of 100 GHz to 700 GHz [12].

The complex baseband signal was then analysed using a systematic DSP procedure containing an adaptive equaliser to provide a suboptimal blind equalisation of time variants of the channel driven by the constant-modulus algorithm (CMA). The technique was devised by Godard in 1980 [16] and is considered one of the most commonly used equalisation methods. We also discuss the synchronisation of the local oscillator (LO) at the receiver with the transmitted signal using the algorithm described in [17].

We then investigated 16-quadrature amplitude modulation (16-QAM) in terms of the optimum amount of optical power to be fed to the emitter, the share of power required from the modulator, and the carrier optical branches required to achieve an optimised 16-QAM signal reception. The QPSK modulation that we used earlier was not suitable for this investigation. The 16-QAM has three IQ levels which makes it easier to monitor the influence of the optical power change on the modulated magnitude. The sub-THz frequency was measured at 260 GHz. The optical modulation branch greatly influenced the linearity of the received symbols in the constellation mapping which, in turn, directly affected the quality of the received signal. For 16-QAM, a fast Fourier transform (FFT)-based estimation algorithm was employed to search for the frequency offset [18].

Real data transmissions test the stability of a system and compare its ability to modulate different types of data points with that of pseudo-random sequences (PRBS). We thus conclude our measurement testbed characterisation with an image transmission demonstration. In this study, we achieved an error-free data reception in the measurement path via QPSK modulation at 25 Gbit/s centred at 260 GHz, a modulated optical frequency of 194.75 THz, and an emitter DC bias of -1V.

The study in this paper focused on the 6G candidate frequency band, which falls within the WR03 waveguide range, from 252.72 GHz to 321.84 GHz, and investigated the influence of data transmission performance and measurement setup parameters on the received signal. This band has received considerable research attention recently as its atmospheric transmission window is around 300 GHz [19]. Frequencies up to 322 GHz have already been standardised by the IEEE 802.15.3d [20].

The IEEE802.15.3d standard allows different channel sizes to be used for different applications [5]. Figure 1 presents the channel allocation of different channel bandwidths according to the IEEE 802.15.3d, showing the frequency bands that this study tested at different modulations. The chosen frequencies correspond to the mid-WR03 waveguide band, which is favourable to achieving the best performance from the waveguide components at the receiver. The QPSK investigation of this present study closely intersects with IEEE 802.15.3d channels 57 to 60. At the same time, the 16-QAM investigation lies between channels 49 and 50. The selected measurement bandwidth and centre frequencies correspond to the optimal settings required, based on the modulation and the different hardware used in the measurement setup, which were validated by the image transmission setup around the 260 GHz frequency band.

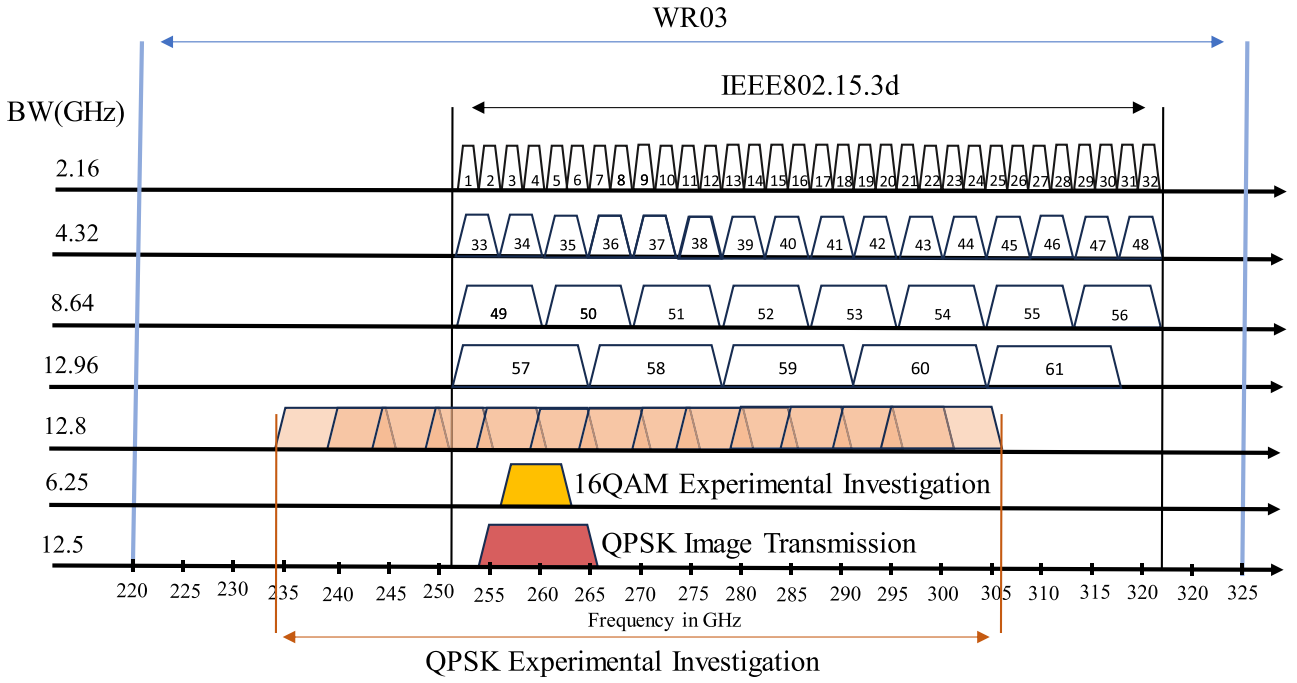

FIGURE 1. Channel allocation proposed by the IEEE 802.15.3d and the frequencies investigated in this present study.

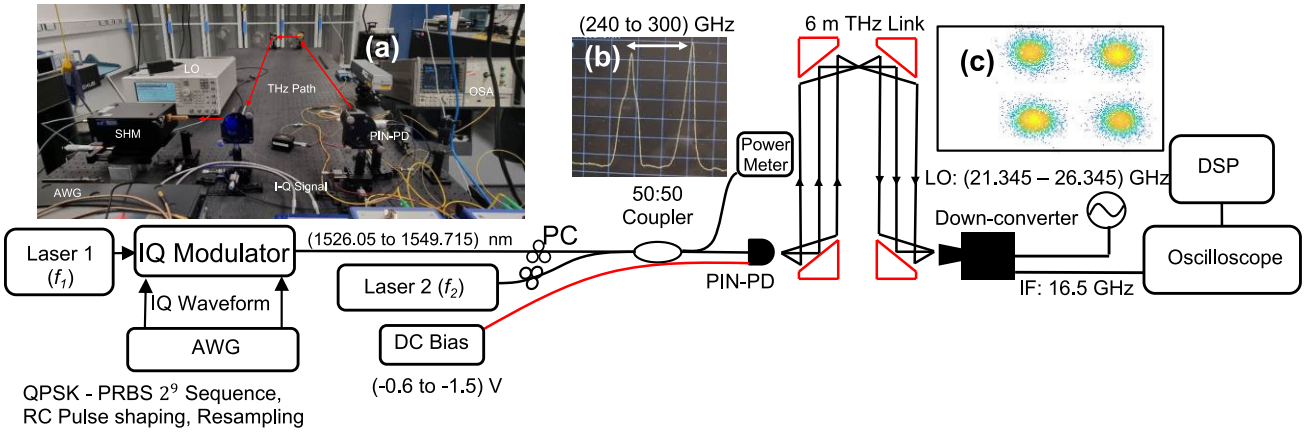

FIGURE 2. Measurement setup. (a) A photograph of the setup, showing the transmission path; (b) the OSA trace of the two optical frequencies; and (c) QPSK constellation received over 6m transmission after DSP.

II. MEASUREMENT SETUP

As seen in Figure 2, the measurement setup depicts a single-channel heterodyne photonic-based THz link. The signal generation comprised two continuous waves distributed feedback (CW-DFB) tuneable laser sources, with wavelengths of 1526.05 nm and 1549.75 nm, using a matrIQ-Laser 1000 Series™ laser source, which offers a linewidth of 100 kHz and tunability resolution of 0.01 pm. The optical frequency separation between the two lasers generated an OTA transmitted THz signal at $f_{THz} = |f_1 - f_2|$, where f_1 and f_2, are the optical frequencies of the tuneable lasers. The f_{THz} was selected between 0.24 THz to 0.3 THz to fit within the WR3.4 receiver band. Figure 2 (a) shows a photograph of the measurement setup and the transmission path. Figure 2 (b) shows the two optical frequencies measured using an optical spectrum analyser (OSA) while Figure 2 (c) shows the error-free QPSK constellation diagram at 25.6 Gbit/s.

One laser was the optical carrier while the other was modulated with the IQ orthogonal components of a complex signal generated by a Coherent Solutions IQ Transmitter-FDP Complex Modulation Transmitter™.

The modulator amplified the electrically separated I and Q components of the signal, that had been generated using a Keysight M8194A™ 120 GSa/s arbitrary waveform generator (AWG); the digitally generated signals were mapped to their oversampled symbols before they were loaded in the AWG.

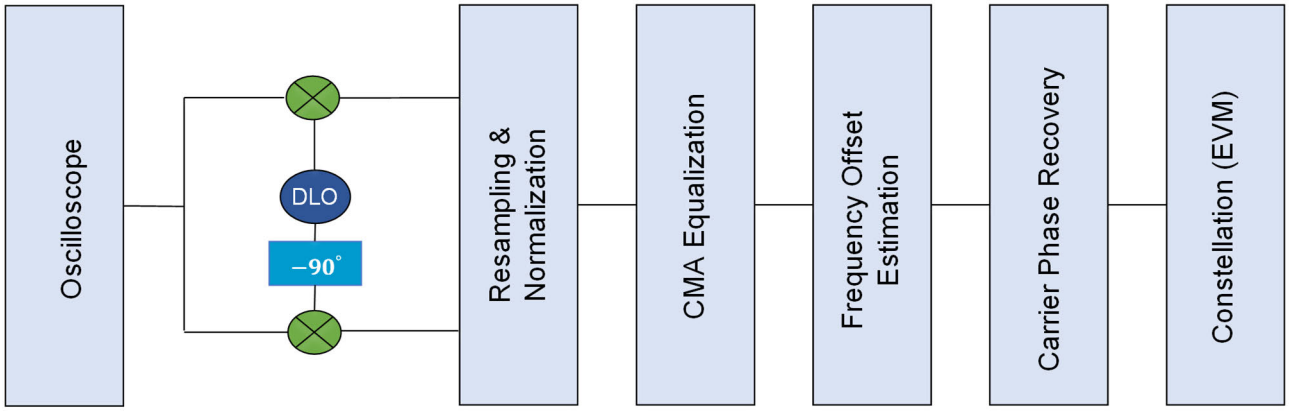

FIGURE 3. DSP blocks used to demodulate the received signals.

The IQ output signals of the AWG were then fed to drive the optical IQ modulator, which converted the data to the optical domain using internal Mach-Zehnder-Modulator (MZM) structures.

The two optical signals were fibre-coupled by a 50% optical coupler prior to launching into a TOPTICA Photonics™ PCA-FD-1550-100-TX-3™ InGaAs PIN-PD photomixer. The two lasers were photomixed and the sub-THz signal was emitted via an internal bow-tie antenna mounted on a hyper-hemispherical silicon lens to produce a beam with 15° full-width half maximum divergence and output power of around 0 dBm for the selected 0.3 THz frequency band, achieving a dynamic range of 90 dB at 100 GHz and 70 dB at 500 GHz, [21].

The THz waveform can be expressed as [22]:

$$Y_{THz}(t) = \eta A_1 A_2 [I\ cos(\omega_{THz} t + \theta_{THz}) + Q\ sin(\omega_{THz} t + \theta_{THz})] \quad (1)$$

where η is the optical mixer conversion efficiency, which includes the influence of the applied DC bias; A_1 and A_2 are the optical amplitudes of the carrier and modulated IQ waveforms, respectively; and ω_{THz} and θ_{THz} are the angular frequency and phase of the generated THz signal, which is the difference between the two optical frequencies. This transmission scheme provided accurate and undistorted frequency conversion of the modulated waveforms, from the optical to the THz range. The signal received at the THz frequency passed through a bandpass filter imposed by the emitter and the receiving waveguide operational range, preventing the image frequencies from accompanying the received signal.

Sub-THz signal transmissions are presumably LoS (line of sight) and require beam directionality towards the receiver. To avoid beam divergence and the associated propagational losses, the transmitted signal was collimated using four parabolic mirrors aligned through two folds of 3 meters to achieve a total distance of 6 meters. A 25 dBi WR3.4 horn antenna was placed at the receiver end and connected to a VDI WR3.4MixAMC™, sub-harmonic mixer (SHM), to detect the received sub-THz signal. The SHM had an IF output bandwidth of 40 GHz and was driven by a 12-time frequency multiplied electrical LO signal. The received waveforms passed through the receiver horn antenna and propagated through the receiving circuit waveguide.

An external synthesizer was used as an LO source. The resulting mid-band IF frequency was within the mid frequency range of the receiving oscilloscope, which can be expressed as:

$$Y_{IF} = A_{IF} [I\ cos(\omega_{IF} t + \theta_{IF}) + Q\ sin(\omega_{IF} t + \theta_{IF})] \quad (2)$$

where A_{IF}, ω_{IF}, θ_{IF} are the amplitude, the angular frequency, and the phase of the IF received waveform, respectively. The recorded waveforms were then prepared for DSP analysis using MATLAB Communications Toolbox™at different demodulation steps to reconstruct the signal received in its original symbols.

III. DIGITAL SIGNAL PROCESSING

Figure 3 shows the block diagram that was used to process the received signal and extract the constellation points onto their mapped positions. After the signal was captured using the oscilloscope at a sampling frequency close to the one used to generate the signal, the recorded block was demodulated and digitally down-converted using a digital LO frequency that matched the IF received to reach the baseband, with the IQ components extracted from the received vector. The digital down-conversion of the received signal can be expressed as:

$$Y_{BB,IQ}(nT_p) = Y_{IF}(cos(\omega_{IF}(nT_p)) - sin(\omega_{IF}(nT_p))) \quad (3)$$

where n is the sample number of N recorded samples and T_p is the sampling period of the digital waveform.

The signal was then down-sampled and digitally lowpass filtered and normalised:

$$Y_{DS,IQ}(nT_p) = \langle Y_{BB,IQ}(nT_p) \rangle * I_L \quad (4)$$

where $(*)$ is the convolution between the filtered IQ waveform and the downsampling I_L unity vector, and L is the

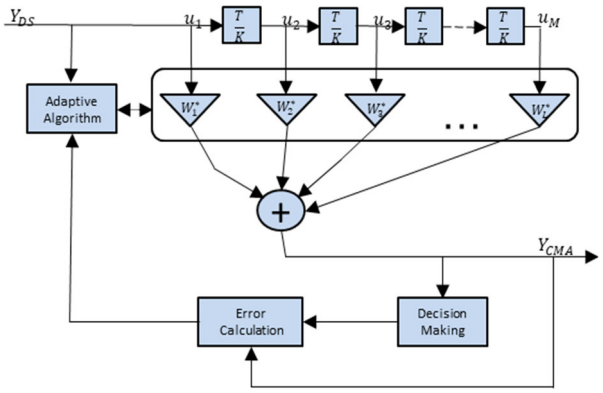

FIGURE 4. A diagram of the CMA equalisation block.

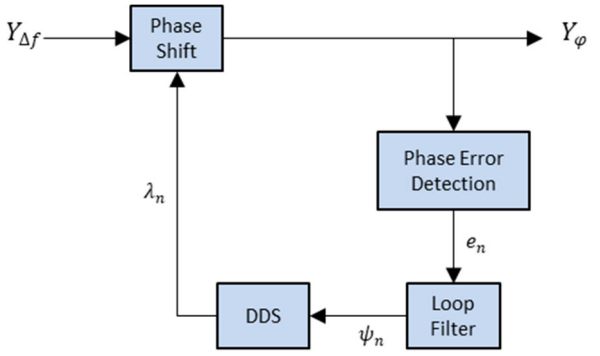

FIGURE 5. The process of the carrier phase recovery.

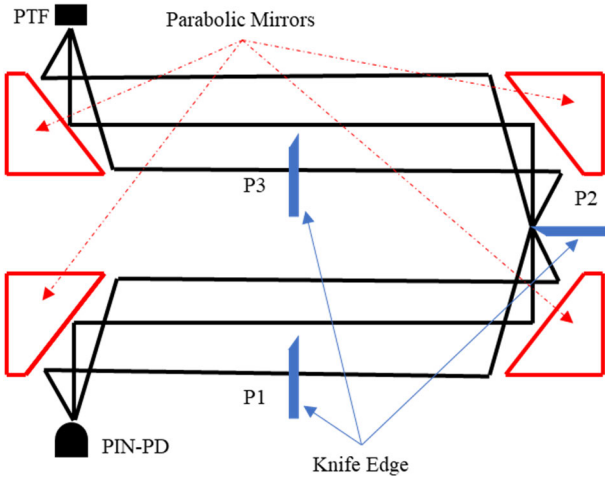

FIGURE 6. The knife edge positions examined along the measurement path.

downsampling factor. The angle brackets represent the digital lowpass filter.

The complex baseband signal was then fed into the CMA equaliser, which is well known for its lower computational complexity compared to other equalisers that require training.

The CMA equaliser minimises the dispersion of the output around a circular contour. The sum of the output weights of the delay line is multiplied by the input symbols and adapts its filter coefficients at each symbol to minimise the symbol position to its circular contour [23]. Figure 4 depicts the equalisation steps.

The equalised symbols were then analysed to identify the frequency offset and characterise the sweeping time of the frequency shift at different measurement recordings and within a single measurement record. An FFT-based estimation algorithm was used to determine the frequency offset [18]. The $Y_{\Delta f}$ search conducted using a periodogram of the m_{th} power of the received signal and is given as:

$$Y_{\Delta f} = \frac{f_{samp}}{N.m} argmax_f \left| \sum_{n=0}^{N-1} Y_{CMA}^m(n) e^{-j2\pi nt/N} \right| \quad (5)$$

and $\left(-\frac{R_{sym}}{2} \leq f \leq \frac{R_{sym}}{2}\right)$ should be satisfied, where m is the modulation order, and R_{sym} is the symbol rate. The basic principle is to search for the frequency, which yields the *mth* power of the time average of the received signal corresponding to periodogram maximisation. A recording time sliding window was also used to calculate the frequency offset shift within the recorded waveforms based on the received signal EVM. Frequency offset correction is essential for optical systems to compensate for the IF frequency offset caused by the frequency hopping that occurs when using free-running DFB laser sources.

The phase error was calculated using the phase error detecting block, where both phases were subtracted using a closed loop (Figure 5) that uses the PLL-based algorithm described in [24]. This yielded the corrected phase offset for the input signal:

$$Y_\varphi = Y_{\Delta f} e^{i\lambda_n} \quad (6)$$

where λ_n is the output of the direct digital synthesis (DDS).

IV. BEAM PROFILE

The beam profile was highly relevant to this measurement as no other beamforming was used at the emitter's output or at the receiver's horn antenna. It was also important because it impacts the energy density. Figure 6 shows the beam profile measurement locations P1, P2, and P3, on the beam path using the knife edge method. This was accomplished by translating a rectangular blade across the sub-THz beam so as to block increasing fractions of the wavefront, and measuring the power received from the PD using a PTF detector placed at the receiver's focal point, connected to a lock-in amplifier.

The collimated beam profiles measured at P1 and P3 on the measurement path were, respectively, 1.5 m and 4.5 m from the PD emitter. Figure 7 (a) shows the power of the beam spot and the error function fit. The intensity values were then derived from their knife edge positions to calculate the Gaussian distribution of the beam profile as first derivative, as shown in Figure 7 (b), where both tested locations exhibited similar beam intensities and profiles, confirming that the beam was well collimated.

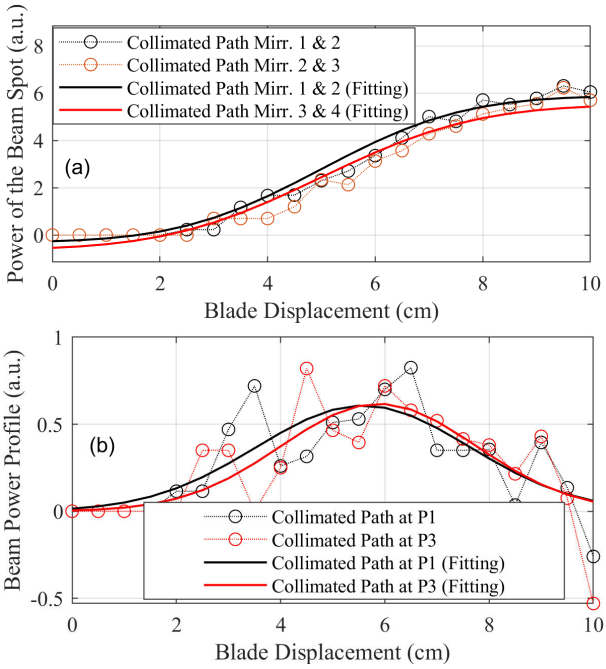

FIGURE 7. The knife edge profile of the PIN-PD collimated path at 260 GHz, optical modulator at 194.75 THz, and bias at −1.5 V. The (a) error function and (b) the derivative and curve fitting.

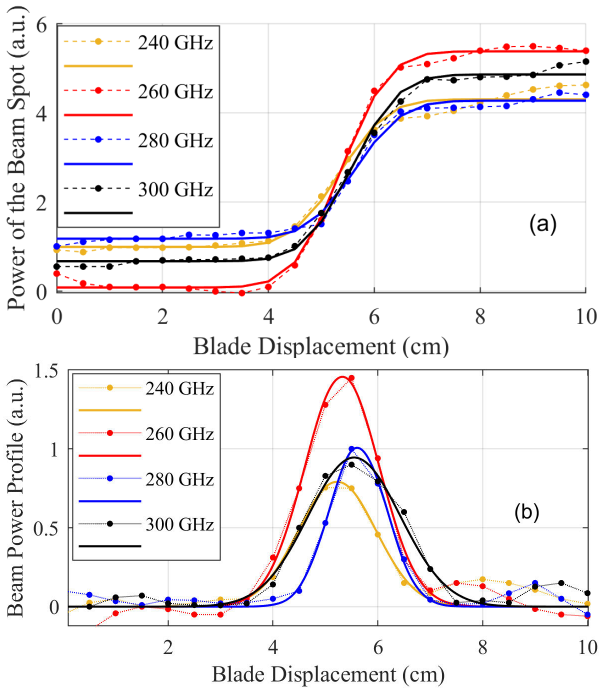

FIGURE 8. The knife edge profile at P2 (a) beam spot size and (b) derivative obtained using the knife edge.

Beam profile measurements were conducted around the focal point at P2. The sub-THz frequencies were tested between 240 GHz and 300 GHz at 20 GHz intervals. The beam profile showed that the power intensity changes from one frequency to another showing its dependance on the measured frequency. The beam profile yielded the highest intensity at a frequency of 260 GHz. Figure 8 (a) shows a sharper drop in power of the beam spot as the focused beam region was affected by the blade displacement. Figure 8 (b) shows the derivative of the measured intensities representing the Gausian distribution of the power profile for the measured sub-THz frequencies.

V. RESULTS AND DISCUSSION

A. QPSK MEASUREMENT

A 2^9 PRBS signal at 12.8 GBaud generated by the IQ AWG output channels at a sampling frequency of 100 Gsa/s, was used for the QPSK measurement. The generated waveform had a raised cosine (RC) pulse-shaping filter with a 0.35 roll-off factor. The IQ baseband signal was then fed to the optical modulator at 500 mV from each of the I and Q channels, producing an optical output power of 3 mW of the modulated waveform coupled with 16 mW from the optical carrier fed to the THz emitter. The down- converter's LO frequency was set between 21.345 GHz and 26.345 GHz to obtain a received IF frequency of 16.5 GHz, depending on the sub-THz frequency transmitted. The received waveforms were recorded using a Keysight-UXR0334A^{TM} real-time oscilloscope (RTO) 128 GSa/s, where the received signal containing 2.56 MSa was split into 160 kSa windows for demodulation analysis.

Additional optical amplifiers were not used at the two optical branches feeding the optical photomixer. The aim was to characterise this setup's measurement parameters and their influence on the received signal quality in terms of the received signal strength and EVM.

Choosing an optical excitation wavelength in the c-band (1530 nm to 1565 nm) facilitated the optimisation of the optical frequency of the setup components, including the DFB laser source, optical modulator, and PD. This optimisation would provide the necessary signal improvement for the best signal reception in terms of signal strength and EVM.

The influence of optical frequency on the received signal was measured by tuning a range of optical frequencies used at the optically modulated branch; specifically, from 193.75 THz to 196.25 THz, at 0.5 THz steps.

The optical carrier frequency was varied to achieve the optically mixed sub-THz band between 240 GHz and 300 GHz at 5 GHz intervals. Figure 9 depicts the performance of the received signal in terms of the signal strength and EVM of the sub-THz frequencies generated using different optical frequency combinations. The peak-to-peak root-mean-square (rms) voltage of the received time-domain signal influenced the optical frequency selection and affected all the sub-THz frequencies. The highest received signal was achieved at 194.75 THz while the lowest was at 196.25 THz, creating a band difference of approximately 0.4 mV.

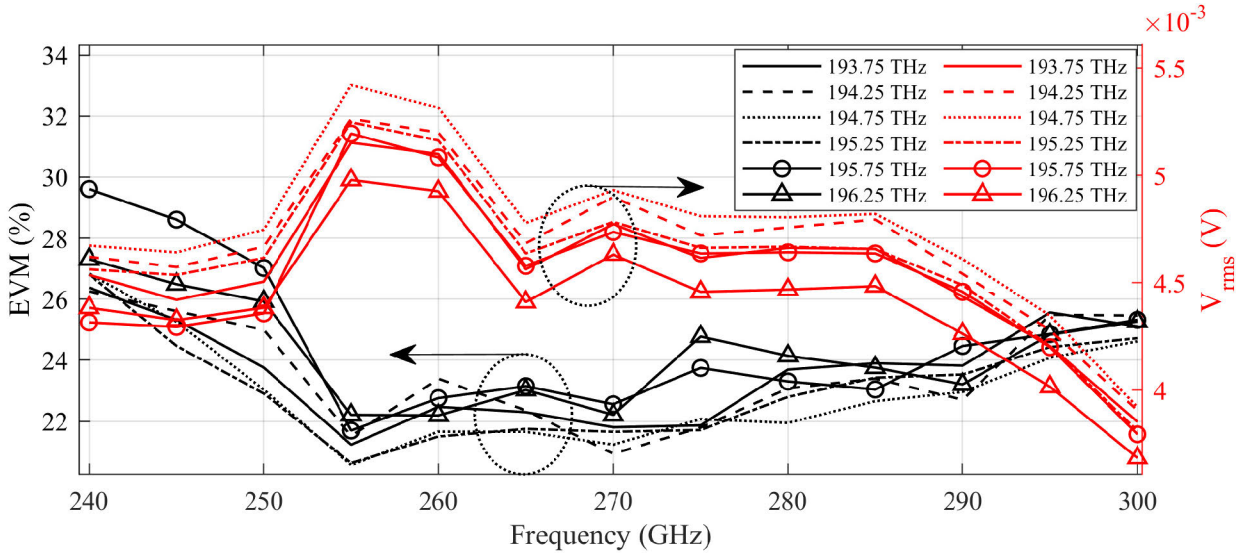

FIGURE 9. The effect of optical frequency on the EVM and strength of the received signal.

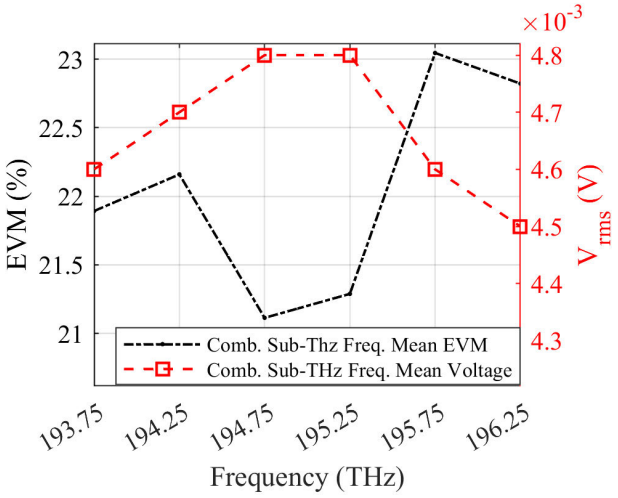

FIGURE 10. The optical frequency vs. the combined root-mean-square (rms) EVM and V_{rms}.

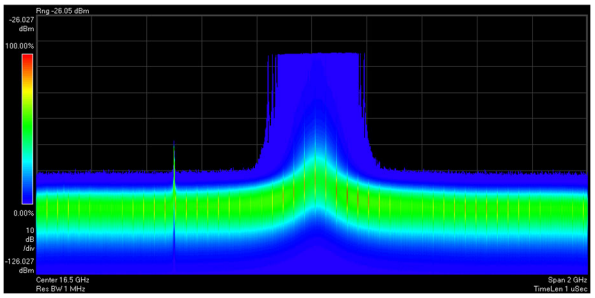

FIGURE 11. Persistent display using the VSA software used by Keysight-UXR0334A^{TM} RTO of the IF down-converted signal around 16.5 GHz, showing the frequency hopping of a single frequency generated by the photomixed lasers.

The EVM reflected this difference less systematically. The best optical frequency performance overlapped depending on the measured sub-THz frequency. Figure 10 shows the mean of the combined sub-THz frequencies for each of the tested optical frequencies. The optical frequency at 194.75 THz outperformed the other frequencies in terms of the strength and EVM of the received signal while the 196.25 THz frequency yielded the weakest signal. However, the 195.75 THz frequency yielded the worst EVM for most of the tested sub-THz frequencies, especially in the lower frequency band.

Different factors affect the stability of propagating signal transmission wavelengths in terms of optical signal generation. Heating and cooling during transmission create instantaneous responses in thermally-tuned laser sources, generating modulation that oscillates around the desired wavelength, which translates to frequency hopping.

The frequency of the present setup drifted by 170 MHz around the down-converted IF. Figure 11 shows a persistent display using PathWave Vector Signal Analysis (VSA) Software, by Keysight's RTO. In this figure, we monitored the frequency hopping effect originated from the laser sources by testing a CW signal down-converted to around the desired 16.5 GHz. Independently from the frequency hopping, all the sub-THz signals had an offset of 360 MHz off the required THz, due to the laser tuning error, which translates to 30 MHz for the applied LO after down-conversion. This offset was compensated at the down-converter to reach the desired 16.5 GHz IF.

The frequency hopping will randomly drift our down-converted modulated signal with a frequency offset, which will be different from one signal recording to another. To be able to perform a proper characterisation for our measurement parameters, we investigated frequency hopping influence on the received waveforms. Figure 12 depicts

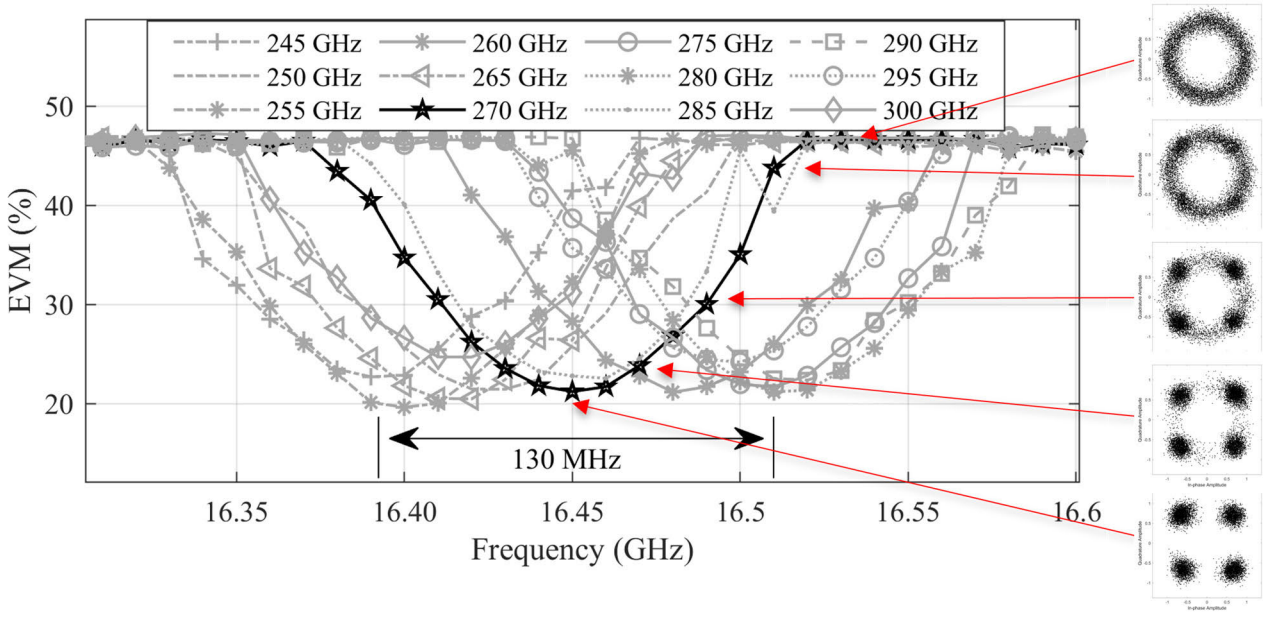

FIGURE 12. A 10 MHz resolution IF step search vs. EVM for down-converted sub-THz waveforms.

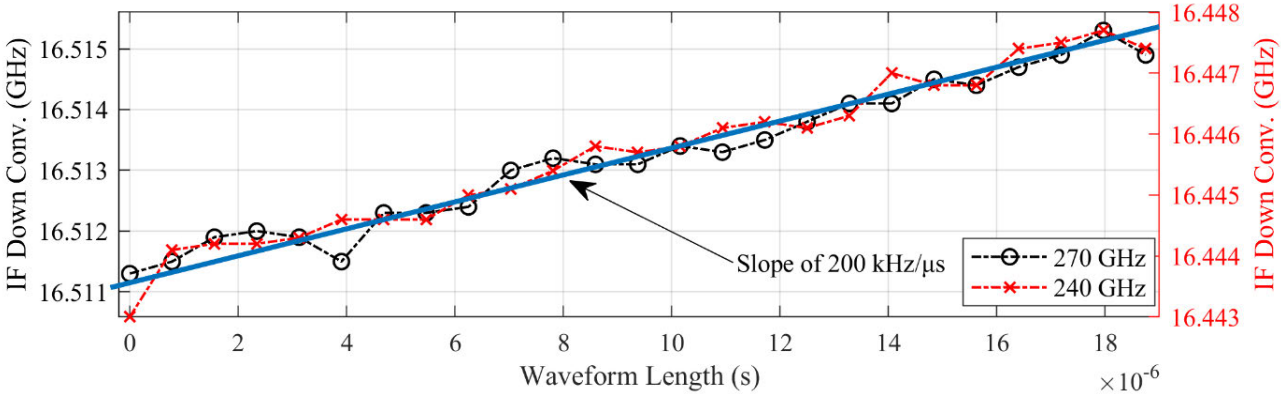

FIGURE 13. The recorded waveform vs. the IF offset slope at 1kHz resolution at down-conversions of 240 GHz and 270 GHz.

the effect of hopping frequency, where a range of sub-THz recorded signals were presented in terms of the EVM at different IFs. The IF offset ranged from 16.39 to 16.52 GHz. A 10 MHz frequency resolution was selected for the EVM calculation. As seen in the figure, 270 GHz is highlighted as an illustrative example. The 270 GHz down-converted IF waveform centred at 16.45 GHz with an off-centre constellations of 20 MHz steps. The EVM reading decreased from 21.22%, where the offset was resolved, compared to 23.57 %, 30.52 %, 40.53 %, and 46.36 % for the off-centre frequency offsets between 20 and 80 MHz. To be able to track the frequency hopping drift and the change in drift amount over time, from one measured signal to another, a 20 μs of continuous data samples were recorded for each parameter tested in our measurement setup. An investigation of the linear sliding window of 1.25 μs was conducted to determine the extent of frequency drift during recording and to calculate the frequency hopping speed and variation of the frequency shift over the recorded duration.

Figure 13 shows the resolved IF frequency of successive 25-time windows of 1.25 μs shifted by 0.78 μs steps to cover the total waveform recording length of 20 μs. The IF was resolved based on the lowest EVM achieved at 1 kHz frequency resolution. Two down-converted frequencies of 270 and 240 GHz were tested and exhibited similar frequency slopes. Both frequencies yielded a total shift of approximately 4 MHz represented by a linear frequency hopping slope of 200 kHz/μs.

The next investigation pertained to the bias DC voltage of the sub-THz emitter. Three reverse-biased voltages, -0.6 V, -1 V, and -1.5 V, were tested for their influence on the received signal strength and EVM.

The DC bias directly affects the output current of the emitter and influences the PD response time, which is important

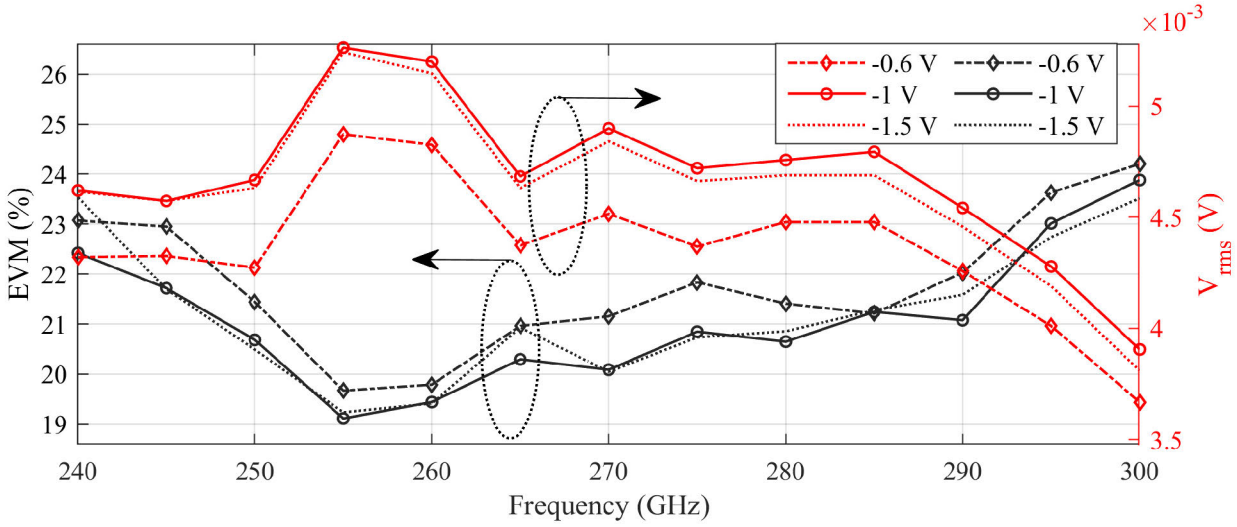

FIGURE 14. The DC Bias vs. Combined RMS EVM and V_{rms}.

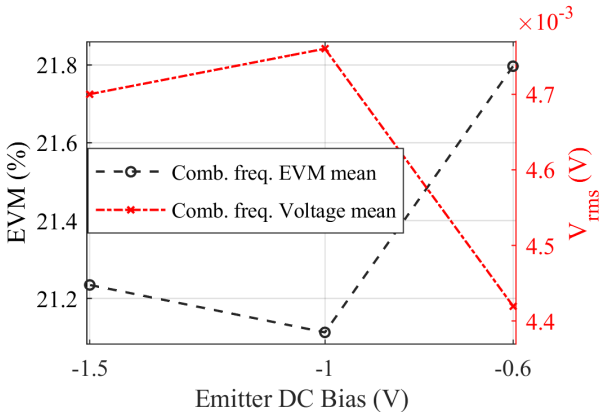

FIGURE 15. The DC Bias vs. Sub-THz frequencies mean in terms of EVM and received signal V_{rms}.

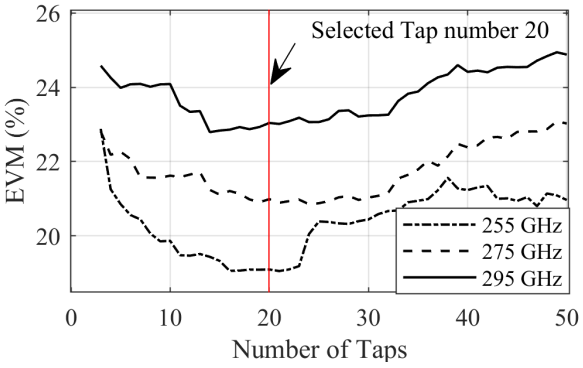

FIGURE 16. CMA equalization number of taps influence on EVM at different sub-THz frequencies.

for modulated optical signals and short pulse applications. As seen in Figure 14, a DC bias of −1 V outperformed voltages of −0.6 V and −1.5 V in terms of EVM and received signal strength. The −1 V bias offered the lowest EVM for most of the tested frequencies and the highest received signal strength for all the sub-THz frequencies under test. Figure 15 depicts the mean calculation of the measured frequencies for rms voltage and of the EVM, where the −1 V bias was the best selection for lowest EVM and highest V_{rms}.

The delay tap selection of the CMA equaliser was examined to improve EVM. A range of taps, between $3-50$, were selected and the EVM output of the entire range of the sub-THz band of interest was calculated.

As seen in Figure 16, the delay tap selection plays an important role for EVM calculation. This was clear as some frequencies are more affected by the tap selection than others, making the mid-band frequency have lower EVM than the band edges. Figure 16 shows how the number of taps influenced three frequencies of 255 GHz, 275 GHz, and 295 GHz. The frequencies of 255 GHz and the 275 GHz start around the same EVM position of 22.8% at Tap 3, yet the two frequencies start to diverge with a difference of around 3% at tap number 20. The equalization delay tap of 20 was selected for our measurement analysis where all the tested frequencies showed convergence to a stable EVM before their EVM rises again with the adaptation taps increase.

B. 16-QAM MEASUREMENT

Some key changes were made to the 16-QAM measurement setup compared to the QPSK measurement setup. This included the addition of erbium-doped fibre amplifier (EDFA), an optical attenuator, and an optical bandpass filter (OBPF) after the output signal of the optical modulator. This change enabled more flexibility in terms of the signal strength produced by the optical modulator branch, which suited the power investigation requirement of this study and enabled the 16-QAM signal to be successfully recovered. The

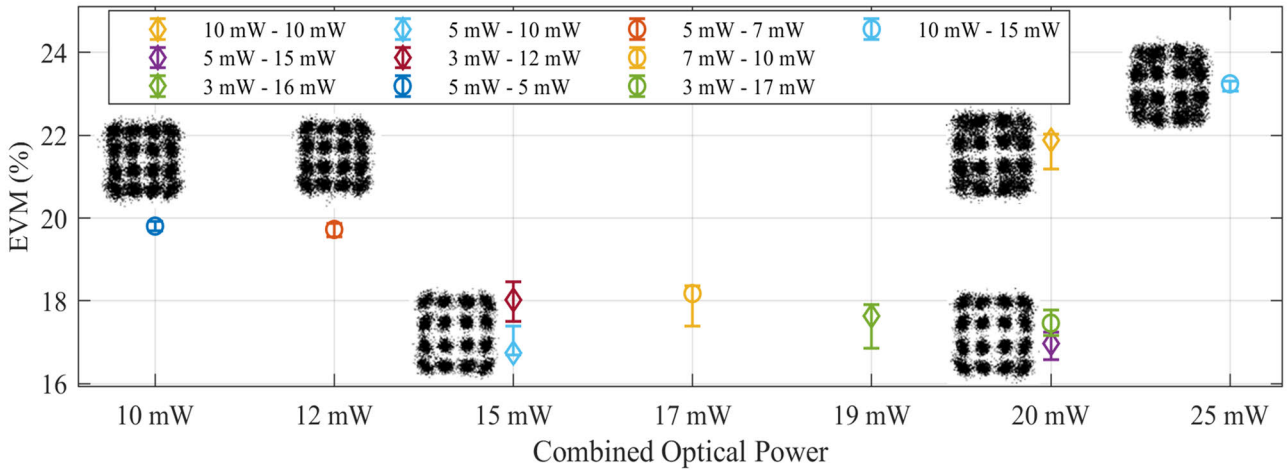

FIGURE 17. The combinations of optical power vs. EVM.

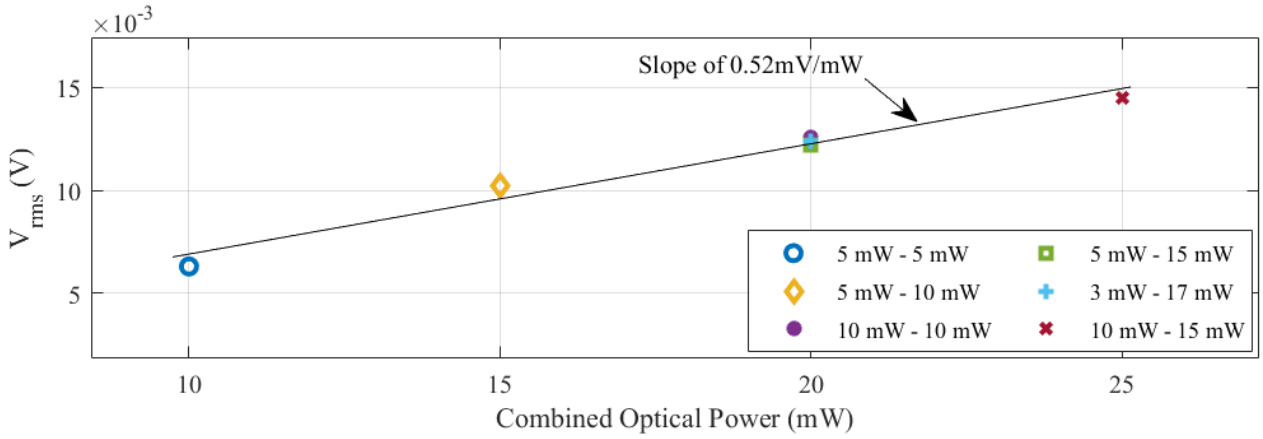

FIGURE 18. The Optical power vs. received signal strength.

waveforms at the receiver side were recorded using a Tektronix™ DPO72304DX – 100 GSa/s. 2 MSa were recorded for each of the investigated waveforms with three repetitions. The generated waveforms were characterised as 25 Gbit/s, 6.25 GHz bandwidth, pulse shaped with RC filter, and 0.35 roll-off factor. The optical frequencies selected for this measurement were 194.75 THz and 194.49 THz, representing the modulated and the carrier frequencies, respectively, forming a propagating 260 GHz OTA modulated signal. The demodulation steps investigated different time widows of 640 kSa sliding at 10 KSa along the whole recording.

The measurement involved determining the optimal amount of optical power to be fed to the emitter and the power share required from the modulated and the carrier optical branches. Figure 17 shows different sets of optical power selections between 10 mW and 25 mW at balanced and unbalanced power combinations. The power values shown were the contributions of the optical modulator versus optical carrier power to the final optical power fed to the emitter. These power levels were essential to guarantee separation between the constellation power levels, especially the outer constellation rings as discussed below.

As seen Figure 17, the 16-QAM constellation points suffered from the effects of noise due to weak signal strength at 10 mW and 12 mW. The EVM began to improve at 15 mW at both combinations of optical power, especially at 5 mW (modulated) and 10 mW (carrier). The figure also shows the three repeated analyses of each setting as error bars. As seen, increasing the modulator's power to more than 5 mW caused an increase in the EVM due to the nonlinearity affecting the transmitted waveform. This was visible at the different 20 mW power combinations, where the 5 mW – 15 mW range shows a 5% difference in EVM compared to the 10 mW – 10 mW combination. Furthermore, increasing the optical carrier power to 15 mW reduced EVM even further.

Figure 18 depicts the relation between the total optical power and the received rms voltage. As seen, increasing the linear voltage caused an increase in the optical power at a slope of 0.52 mV/mW. Furthermore, unlike EVM, different

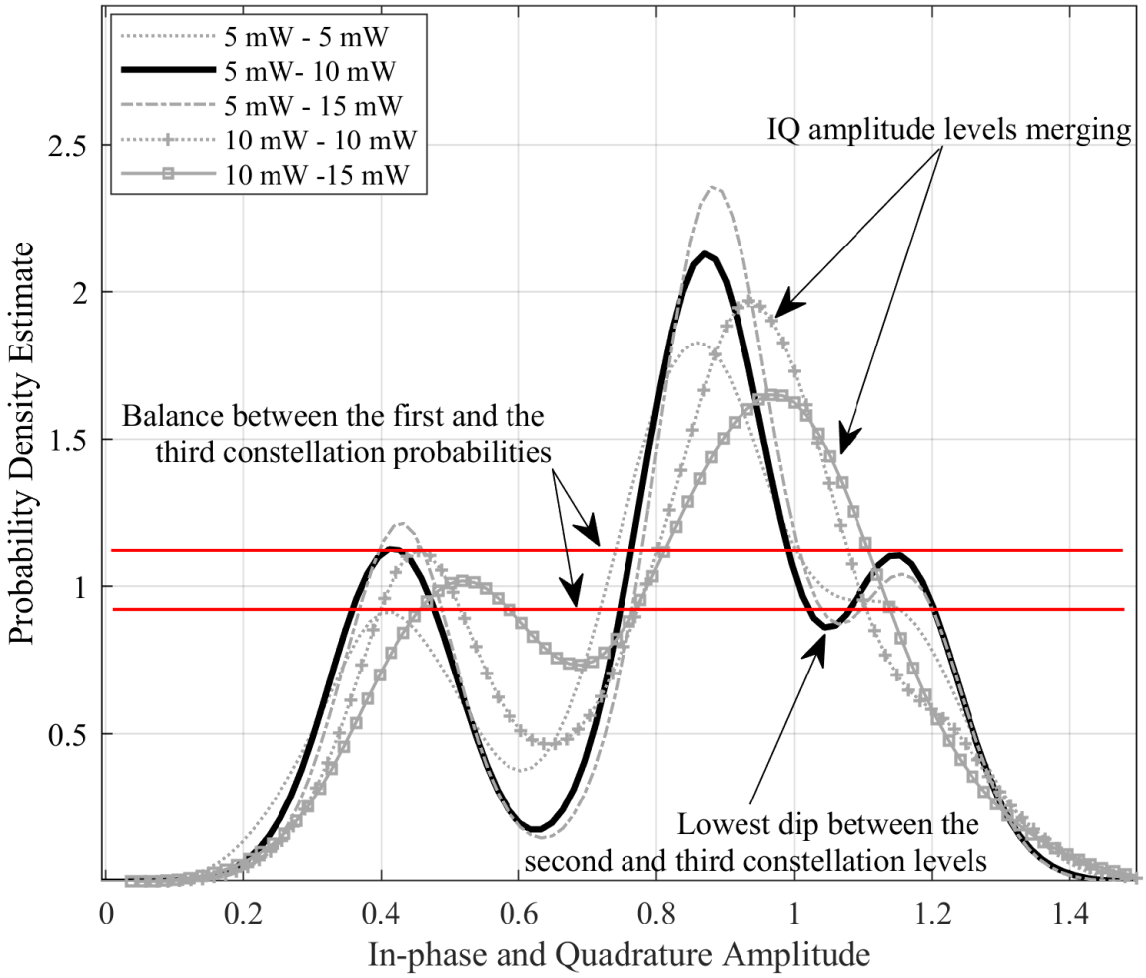

FIGURE 19. The IQ Amplitude vs. density distribution at different combinations of optical power.

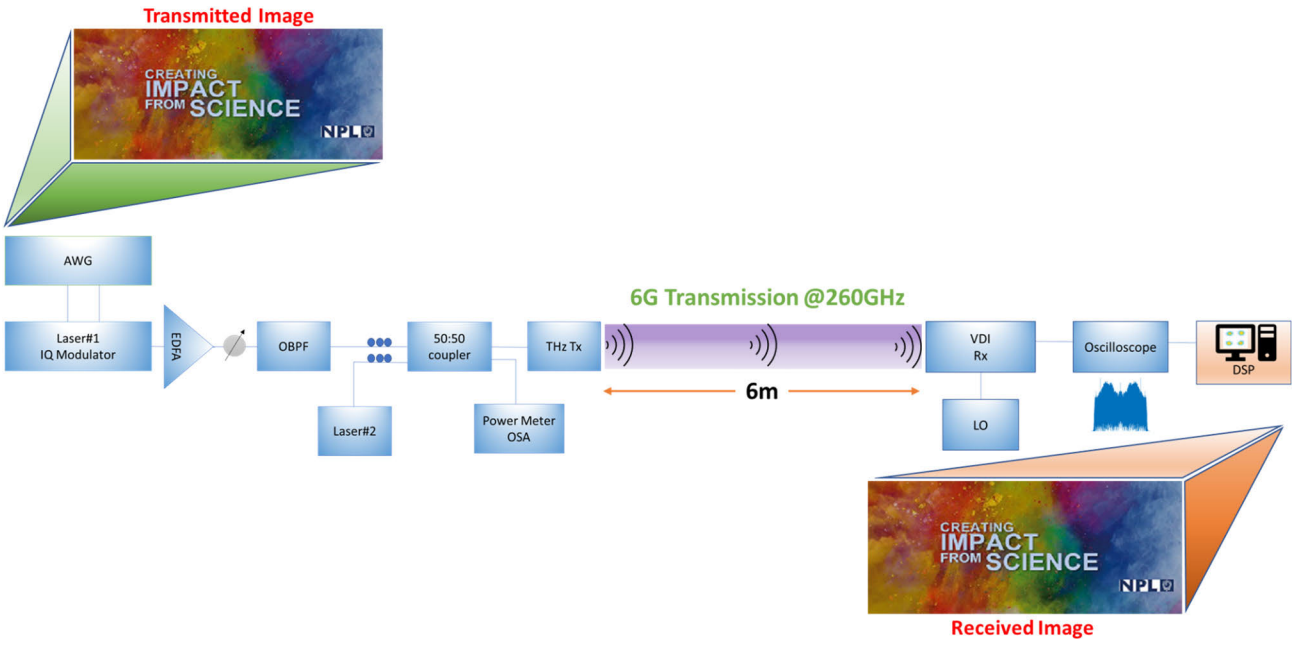

FIGURE 20. The transmitted image and the image transmission measurement setup.

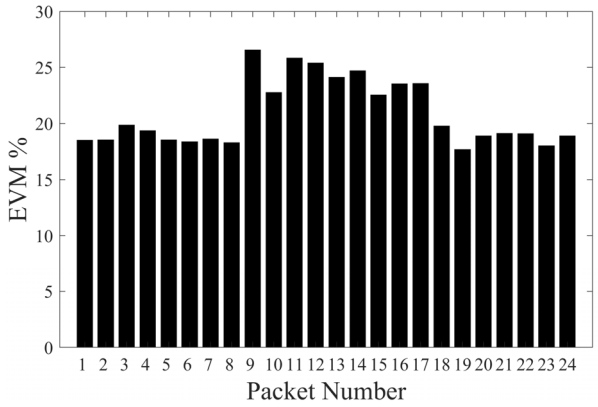

FIGURE 21. The RMS EVM of the received image packets.

power combinations provided a similar level of received rms voltage.

The optical power combination of the IQ amplitude and the probability density estimate of the 16-QAM signal have been examined in Figure 19. The probability density estimate indicates the optical power needed to reach the expected symbol probability at each constellation amplitude level. The lowest and highest levels for the PRBS 16-QAM modulated signal should possess similar symbol probabilities that represent the four constellation points at each level. As seen, at power combinations of 5 mW − 5 mW and 5 mW − 10 mW, increasing the optical carrier power branch to 15 mW affected the balance of the two levels.

On the other hand, increasing the modulated optical power to 10 mW affected the IQ amplitude represented by the amplitude levels of the 16-QAM constellation points.

As seen in Figure 19, the outer points of a 16-QAM constellation are more affected than the inner constellation points by nonlinearities in IQ amplitude induced by the influence of over scaling caused by reaching the PD's non-linear region. The best separation between the outer levels was achieved at power combinations of 5mW – 10mW and 5mW – 15 mW.

The 10 mW – 10 mW and 10 mW – 15 mW power combinations suffered a shifted IQ amplitude. The symbol's amplitude in the received constellation diagram shows that symbols mapped at the inner constellation levels shifted more than the outer level, causing the outer IQ levels to merge.

C. IMAGE TRANSMISSION

Figure 20 depicts the measurement setup used to test the image transmission. The image had to be sampled to its digital bits and mapped to IQ symbols to perform this task. A QPSK modulation at 12.5 Gbaud and centered at 260 GHz with a modulated optical frequency of 194.75 THz and an emitter's DC bias of −1 V was used for the measurement.

To work around the memory limitations of the AWG, the transmission symbols were divided into 24 packets containing 55296 IQ symbols oversampled by a factor of eight, carrying 442368 samples equally in each packet. The selected number of samples was less than the maximum 524288 samples that the AWG can transmit at a time. It also contained a 3456-multiplication factor of the 128 samples that the AWG requires to saturate the transmission bus feed with samples for each channel used. Otherwise, padding or truncating needs to be applied. Figure 21 depicts the packet reception EVM percentage, where no errors were detected. The EVM fluctuations depended on the binary representation of each segmented packet and the 0 and 1 distributions in each measured packet. The more bits distribution achieved the better stability the optical modulator's amplifier would have, and the lower the EVM percentage is achieved for the received packet. The received bits were identical to the transmitted bits for all the 24 packets of the image data transmitted over 6 m, demonstrating error-free transmission at 260 GHz, which is a frequency of interest for 6G research.

VI. CONCLUSION

This study set up and tested a single-channel heterodyne photonic-based sub-THz link using four parabolic mirrors aligned in two folds of 3m− distance to achieve a total distance of 6m. Several parameters were investigated to improve and optimise data transmission and to yield optimal signal transmission.

The investigation involved different sub-THz frequencies within the WR03 band.

For the QPSK measurement setup, the investigated frequencies showed a deviation in EVM and received signal strength, providing the best performance between 255 to 270 GHz. The tested optical frequencies gave the best performance at 194.75 THz. Three emitter bias voltages were investigated and showed a clear improvement in rms voltage of the received signal and rms EVM percentage at -1 V compared to −0.6 and −1.5 V.

The frequency hopping from laser sources caused a back-and-forth frequency drift of 170 MHz. The drift investigated for different measurement recordings and along a single measurement of 20μs showed the possibility of detecting a 200 kHz/μs frequency change using EVM readings as a reference.

A 16-QAM measurement was performed to examine the effect of the optical power of the two optical branches on the received constellation diagram. The 5 mW 10 mW and 5 mW 15 mW power combinations performed best compared to other power combinations we tested.

An error-free image transmission was achieved by converting the image data into 24 packets containing 55296 IQ symbols oversampled by a factor of eight and carrying 442368 samples in each packet equally.

ACKNOWLEDGMENT

The authors would like to declare that they have no conflicts of interest to disclose.

REFERENCES

[1] S. Kim, J. Yun, D. Yoon, M. Kim, J.-S. Rieh, M. Urteaga, and S. Jeon, "300 GHz integrated heterodyne receiver and transmitter with on-chip fundamental local oscillator and mixers," *IEEE Trans. Terahertz Sci. Technol.*, vol. 5, no. 1, pp. 92–101, Jan. 2015.

[2] J.-D. Park, S. Kang, S. V. Thyagarajan, E. Alon, and A. M. Niknejad, "A 260 GHz fully integrated CMOS transceiver for wireless chip-to-chip communication," in *Proc. Symp. VLSI Circuits (VLSIC)*, Jun. 2012, pp. 48–49.

[3] I. Kallfass, F. Boes, T. Messinger, J. Antes, A. Inam, U. Lewark, A. Tessmann, and R. Henneberger, "64 Gbit/s transmission over 850 m fixed wireless link at 240 GHz carrier frequency," *J. Infr., Millim., Terahertz Waves*, vol. 36, no. 2, pp. 221–233, Feb. 2015.

[4] N. Sarmah, J. Grzyb, K. Statnikov, S. Malz, P. R. Vazquez, W. Föerster, B. Heinemann, and U. R. Pfeiffer, "A fully integrated 240-GHz direct-conversion quadrature transmitter and receiver chipset in SiGe technology," *IEEE Trans. Microw. Theory Techn.*, vol. 64, no. 2, pp. 562–574, Feb. 2016.

[5] M. Fujishima, "Overview of sub-terahertz communication and 300 GHz CMOS transceivers," *IEICE Electron. Exp.*, vol. 18, no. 8, 2021, Art. no. 20212002.

[6] A. Kanno, K. Inagaki, I. Morohashi, T. Sakamoto, T. Kuri, I. Hosako, T. Kawanishi, Y. Yoshida, and K.-I. Kitayama, "20-Gb/s QPSK W-band (75–110 GHz) wireless link in free space using radio-over-fiber technique," *IEICE Electron. Exp.*, vol. 8, no. 8, pp. 612–617, 2011.

[7] X. Pang, A. Caballero, A. Dogadaev, V. Arlunno, R. Borkowski, J. S. Pedersen, L. Deng, F. Karinou, F. Roubeau, D. Zibar, and X. Yu, "100 Gbit/s hybrid optical fiber-wireless link in the W-band (75–110 GHz)," *Opt. Exp.*, vol. 19, no. 25, pp. 24944–24949, 2011.

[8] Y. Yoshimizu, S. Hisatake, S. Kuwano, J. Terada, N. Yoshimoto, and T. Nagatsuma, "Wireless transmission using coherent terahertz wave with phase stabilization," *IEICE Electron. Exp.*, vol. 10, no. 18, 2013, Art. no. 20130578.

[9] T. Harter, S. Ummethala, M. Blaicher, S. Muehlbrandt, S. Wolf, M. Weber, M. M. H. Adib, J. N. Kemal, M. Merboldt, F. Boes, and S. Nellen, "Wireless THz link with optoelectronic transmitter and receiver," *Optica*, vol. 6, no. 8, pp. 1063–1070, 2019.

[10] S. Nellen, S. Lauck, G. Schwanke, M. Deumer, R. B. Kohlhaas, L. Liebermeister, M. Schell, and B. Globisch, "Radiation pattern of planar optoelectronic antennas for broadband continuous-wave terahertz emission," *Opt. Exp.*, vol. 29, no. 6, pp. 8244–8257, 2021.

[11] R. Müller, W. Bohmeyer, M. Kehrt, K. Lange, C. Monte, and A. Steiger, "Novel detectors for traceable THz power measurements," *J. Infr., Millim., Terahertz Waves*, vol. 35, no. 8, pp. 659–670, Aug. 2014.

[12] S. Nellen, T. Ishibashi, A. Deninger, R. B. Kohlhaas, L. Liebermeister, M. Schell, and B. Globisch, "Experimental comparison of UTC- and PIN-photodiodes for continuous-wave terahertz generation," *J. Infr., Millim., Terahertz Waves*, vol. 41, no. 4, pp. 343–354, Apr. 2020.

[13] G. Liu, G. Zhao, J. Sun, D. Gao, Q. Lu, and W. Guo, "Experimental demonstration of DFB lasers with active distributed reflector," *Opt. Exp.*, vol. 26, no. 23, p. 29784, 2018.

[14] J. Smith, M. Naftaly, S. Nellen, and B. Globisch, "Beam profile characterisation of an optoelectronic silicon lens-integrated PIN-PD emitter between 100 GHz and 1 THz," *Appl. Sci.*, vol. 11, no. 2, p. 465, Jan. 2021.

[15] T. A. Heumier, "Mode hopping in semiconductor lasers," Ph.D. dissertation, Dept. Phys., Montana State Univ., Bozeman, MT, USA, 1992.

[16] D. Godard, "Self-recovering equalization and carrier tracking in two-dimensional data communication systems," *IEEE Trans. Commun.*, vol. COM-28, no. 11, pp. 1867–1875, Nov. 1980.

[17] M. Rice, *Digital Communications: A Discrete-Time Approach*. London, U.K.: Pearson, 2009.

[18] Y. Wang, K. Shi, and E. Serpedin, "Non-data-aided feedforward carrier frequency offset estimators for QAM constellations: A nonlinear least-squares approach," *EURASIP J. Adv. Signal Process.*, vol. 2004, pp. 1–9, Dec. 2004.

[19] *Attenuation by Atmospheric Gases*, document ITU-R 676-10, International Telecommunication Union, 2016.

[20] V. Petrov, T. Kurner, and I. Hosako, "IEEE 802.15.3D: First standardization efforts for sub-terahertz band communications toward 6G," *IEEE Commun. Mag.*, vol. 58, no. 11, pp. 28–33, Nov. 2020, doi: 10.1109/MCOM.001.2000273.

[21] Toptica. *GaAs and InGaAs Photomixers*. Accessed: Oct. 1, 2023. [Online]. Available: https://www.toptica.com/products/terahertz-systems/frequency-domain/gaas-and-ingaas-photomixers

[22] X. Pang, O. Ozolins, S. Jia, L. Zhang, R. Schatz, A. Udalcovs, V. Bobrovs, H. Hu, T. Morioka, Y.-T. Sun, J. Chen, S. Lourdudoss, L. K. Oxenløwe, S. Popov, and X. Yu, "Bridging the terahertz gap: Photonics-assisted free-space communications from the submillimeter-wave to the mid-infrared," *J. Lightw. Technol.*, vol. 40, no. 10, pp. 3149–3162, May 2022.

[23] D. L. Jones, "A normalized constant-modulus algorithm," in *Proc. 29th Asilomar Conf. Signals, Syst. Comput.*, 1995, pp. 694–697.

[24] M. Rice, *Digital Communications: A Discrete-Time Approach*. NJ, USA: Pearson Education Inc, 2009.

MOHANAD DAWOOD AL-DABBAGH (Member, IEEE) was born in Baghdad, Iraq. He received the B.Sc. degree in electrical engineering from Al-Mustansiriya University, Iraq, in 2006, and the M.Sc. degree in wireless communications engineering for radar systems signal generation and received signal de-noising from University Putra Malaysia, Malaysia, in 2013. He is currently pursing the Ph.D. degree in investigating the implementation of traceable measurement variables for sub-THz communications: development of calibration standards for VNA and channel sounding systems with Physikalisch-Technische Bundesanstalt (PTB), Braunschweig. He was a Guest Researcher with NPL. He worked as a Communications Engineer and as a University Lecturer for several years at different universities in Iraq. He also worked in research projects in Malaysia and Germany.

JESSICA SMITH received the joint Ph.D. degree from the University of Surrey and the National Physical Laboratory (NPL), with a focus on scanning near-field optical microscopy (SNOM) and THz source characterization. She has been a Higher Scientist with the National Physical Laboratory, since 2022. Her current research interests include telecoms applications, including THz communications, antenna characterisation, and mobile networks.

THOMAS KLEINE-OSTMANN was born in Lemgo, Germany, in 1975. He received the M.Sc. degree in electrical engineering from the Virginia Polytechnic Institute and State University, Blacksburg, VA, USA, in 1999, the Dipl.-Ing. and Dr.-Ing. degrees in radio frequency engineering from Technische Universität (TU) Braunschweig, Germany, in 2001 and 2005, respectively, and the Habilitation degree in radio frequency engineering.

Since 2006, he has been a Permanent Scientist with the Electromagnetic Fields Group, PTB, Braunschweig. In 2007, he was the Head of the Electromagnetic Fields Group; the Electromagnetic Fields and Antenna Measuring Techniques Group, in 2012; and the Department High Frequency and Electromagnetic Fields, in 2020. He has been a Lecturer with TU Braunschweig, since 2007. After the Habilitation degree, he was an External Faculty Member with Privatdozent, in 2014. Currently, he is working on realization and transfer of the electromagnetic field strength, electromagnetic compatibility, antenna measuring techniques, and THz metrology. He is giving lectures on microwave and wireless metrology. He is a member of VDE and URSI. He received the Kaiser-Friedrich Research Award, in 2003, for his work on a continuous-wave THz imaging systems.

MIRA NAFTALY is currently with the National Physical Laboratory, U.K.

IRSHAAD FATADIN (Senior Member, IEEE) is currently a Principal Scientist with the Electromagnetic Technologies Group, National Physical Laboratory (NPL). He is also a Visiting Professor with the Faculty of Engineering and Physical Sciences, University of Surrey. He leads NPL's collaborative research with industry and academia on several projects in the telecoms area. He is a Chartered Physicist (CPhys), a Chartered Engineer (CEng), and registered with the Engineering Council, U.K.